

Generalized characteristic relaxation boundary conditions for unsteady compressible flow simulations



Sergio Pirozzoli ^{a,*}, Tim Colonius ^b

^a Università di Roma “La Sapienza”, Dipartimento di Ingegneria Meccanica e Aerospaziale, via Eudossiana 18, 00184 Rome, Italy

^b Division of Engineering and Applied Science, California Institute of Technology, Pasadena, CA 91125, USA

ARTICLE INFO

Article history:

Received 11 October 2012

Received in revised form 25 March 2013

Accepted 10 April 2013

Available online 28 April 2013

Keywords:

Numerical boundary conditions

Compressible flows

Characteristic decomposition

ABSTRACT

We develop numerical boundary conditions for the compressible Navier–Stokes equations based on a generalized relaxation approach (GRCBC), which hinges on locally one-dimensional characteristic projection at the computational boundaries, supplemented with available information from the flow exterior. The basic idea is to estimate the amplitude of incoming characteristic waves through first-order one-sided finite-difference approximations which involve the value of the reference flow state at the first exterior (ghost) point. Unlike other characteristic-based relaxation methods, the present one requires minimal user-supplied input, including the reference flow state, which may be totally or partially known, and in general may vary both in space and time. Furthermore, it can be applied to any type of computational boundary, either inflow or outflow, either subsonic or supersonic. The method is theoretically predicted to convey reduced reflection of waves at computational boundaries compared to other ones, and to have better properties of frequency response to injected disturbances. Numerical tests confirm the improvement of the non-reflecting performance, and demonstrate high degree of flexibility, also for problems with non-trivial far-field boundary conditions (e.g. flows in rotating reference frames) and for the artificial stimulation of subsonic turbulent boundary layers.

© 2013 Elsevier Inc. All rights reserved.

1. Introduction

The specification of suitable numerical conditions at far-field boundaries is a crucial issue for the global accuracy and robustness of compressible Navier–Stokes solvers, since over- or under-prescription of numerical boundary conditions may lead to mathematical ill-posedness of the problem [1]. In practical applications, the main goal of numerical boundary conditions is to allow outgoing disturbances to leave the computational domain with the least possible signature in the interior. Let us consider the Navier–Stokes equations cast in divergence form

$$\frac{\partial \mathbf{u}}{\partial t} + \sum_{i=1}^3 \frac{\partial \mathbf{f}_i}{\partial x_i} = \sum_{i=1}^3 \frac{\partial \mathbf{f}_i''}{\partial x_i}, \quad (1)$$

where

$$\mathbf{u} = \begin{bmatrix} \rho \\ \rho u_j \\ \rho E \end{bmatrix}, \quad \mathbf{f}_i = \begin{bmatrix} \rho u_i \\ \rho u_i u_j + p \delta_{ij} \\ \rho u_i H \end{bmatrix}, \quad \mathbf{f}_i'' = \begin{bmatrix} 0 \\ \sigma_{ij} \\ \sigma_{ik} u_k - q_i \end{bmatrix}, \quad j = 1, 2, 3, \quad (2)$$

* Corresponding author. Tel.: +39 06 44585202; fax: +39 06 44585250.

E-mail address: sergio.pirozzoli@uniroma1.it (S. Pirozzoli).

are, respectively, the vector of conservative variables, and the vectors of the convective and viscous fluxes in the i th direction. Here ρ is the density, u_i is the velocity component in the i th coordinate direction, p is the thermodynamic pressure, $E = e + \rho u^2/2$ is the total energy per unit mass, $e = RT/(\gamma - 1)$ is the internal energy per unit mass, $H = E + p/\rho$ is the total enthalpy, R is the gas constant, $\gamma = c_p/c_v$ is the specific heat ratio, σ_{ij} is the viscous stress tensor, and q_i is the heat flux vector.

A widely used approach to determine artificial boundary conditions for the set of Eqs. (1) was initiated by Thompson [2], which consists in performing a characteristic decomposition in the direction normal to the computational boundary. Referring for instance to a boundary normal to the x direction, the governing equations at the (left and right) mesh boundaries are recast as

$$\frac{\partial \mathbf{u}}{\partial t} + \mathbf{R}_x \Lambda_x \mathbf{L}_x \frac{\partial \mathbf{u}}{\partial x} = \mathbf{C}, \quad (3)$$

where $\Lambda_x = \text{diag } \lambda_\ell$ ($\lambda_1 = u - c$, $\lambda_2 = \lambda_3 = \lambda_4 = u$, $\lambda_5 = u + c$) is the diagonal matrix of the eigenvalues of the Jacobian matrix $\mathbf{A}_x = \partial \mathbf{f}_x / \partial \mathbf{u}$, \mathbf{R}_x and \mathbf{L}_x are the associated matrices of the right and left eigenvectors, and the contributions of the transverse inviscid fluxes and the viscous fluxes are lumped together in the right-hand-side term. A comprehensive list of the transformation matrices involved with characteristic decompositions can be retrieved, e.g. in [3,4], to which we refer for notational purposes. The main idea of the Navier–Stokes characteristic boundary conditions (NSCBC) approach is to isolate the contribution of waves exiting the computational domain, which can therefore be extrapolated from the interior, from those associated with incoming waves, whose amplitude depends on the flow properties outside the computational domain. Let n_x be the x component of the outer normal to the computational boundary ($n_x = -1$ for the left boundary, $n_x = +1$ for the right boundary), this is easily achieved by splitting the eigenvalue matrix into outgoing and incoming parts $\Lambda_x = \Lambda_x^o + \Lambda_x^i$, as follows

$$\lambda_\ell^{o,i} = 1/2(\lambda_\ell \pm n_x |\lambda_\ell|), \quad \ell = 1, \dots, 5. \quad (4)$$

In the case that no information is known from the outside, a common approach is to set to zero the contribution of waves entering the domain, which amounts to assuming $\Lambda_x^i = 0$, thus replacing Eq. (3) with

$$\frac{\partial \mathbf{u}}{\partial t} + \mathbf{R}_x \Lambda_x^o \mathbf{L}_x \frac{\partial \mathbf{u}}{\partial x} = \mathbf{C}, \quad (5)$$

which can be semi-discretized at the boundary node b as

$$\frac{d\mathbf{u}_b}{dt} = -\mathbf{R}_x \Lambda_x^o \mathbf{L}_x D_u \mathbf{u}_b + \mathbf{C}_b, \quad (6)$$

where all matrices are assumed to be evaluated at $x = x_b$, and D_u denotes any one-sided discrete difference operator applied to grid values of \mathbf{u} in the interior of the computational domain. This approach will be referred to as NRCBC (purely nonreflecting) in the following.

Often times (at least partial) information is available on the behavior of the true solution outside the computational domain. In that case, a general strategy to estimate the contribution of the incoming waves was proposed by Poinso and Lele [3], who started from Eq. (3) cast in terms of primitive variables,

$$\frac{\partial \mathbf{v}}{\partial t} + \mathbf{P}^{-1} \mathbf{R}_x \mathcal{L} = \mathbf{P}^{-1} \mathbf{C}, \quad (7)$$

where $\mathbf{P} = \partial \mathbf{u} / \partial \mathbf{v}$ is the Jacobian matrix of the transformation of variables, and the vector

$$\mathcal{L} = \Lambda_x \mathbf{L}_x \frac{\partial \mathbf{u}}{\partial x} = \Lambda_x \mathbf{L}_x \mathbf{P} \frac{\partial \mathbf{v}}{\partial x} = \begin{bmatrix} \lambda_1 \left(\frac{\partial p}{\partial x} - \rho c \frac{\partial u}{\partial x} \right) \\ \lambda_2 \left(c^2 \frac{\partial \rho}{\partial x} - \frac{\partial p}{\partial x} \right) \\ \lambda_3 \frac{\partial v}{\partial x} \\ \lambda_4 \frac{\partial w}{\partial x} \\ \lambda_5 \left(\frac{\partial p}{\partial x} + \rho c \frac{\partial u}{\partial x} \right) \end{bmatrix}, \quad (8)$$

yields the time variation of the characteristic variables, implicitly defined by

$$\partial \mathbf{w} = \mathbf{L}_x \partial \mathbf{u}. \quad (9)$$

The locally inviscid one-dimensional (LODI) approach of [3] amounts to disregarding the contribution of the viscous and transverse terms in Eq. (7) to estimate the components of \mathcal{L} . The resulting system of primitive equations is

$$\begin{cases} \frac{\partial p}{\partial t} + \frac{1}{c^2} [\mathcal{L}_2 + \frac{1}{2}(\mathcal{L}_1 + \mathcal{L}_5)] = 0, \\ \frac{\partial u}{\partial t} + \frac{1}{2\rho c} (\mathcal{L}_5 - \mathcal{L}_1) = 0, \\ \frac{\partial v}{\partial t} + \mathcal{L}_3 = 0, \\ \frac{\partial w}{\partial t} + \mathcal{L}_4 = 0, \\ \frac{\partial p}{\partial t} + \frac{1}{2} (\mathcal{L}_1 + \mathcal{L}_5) = 0, \end{cases} \quad (10)$$

which can be exploited to determine the characteristic wave amplitudes as a function of the time derivative of the primitive variables at the computational boundary. Many practical examples of enforcement of numerical boundary conditions through the LODI approach were given by Poinso and Lele [3].

Another commonly used procedure to determine the amplitude of the incoming characteristic waves is to assume relaxation to the far field conditions. For instance, in the case of subsonic outflow, Poinso and Lele [3] noted that straightforward application of nonreflecting numerical boundary conditions may lead to numerical drift in the long term, since the free-stream value of pressure is not necessarily preserved. To circumvent the pressure drift phenomenon those authors modeled the amplitude of the incoming acoustic wave after Rudy and Strikwerda [5],

$$\mathcal{L}_1 = K_p(p_b - p^*), \quad (11)$$

where p^* is the target value of the pressure (i.e. its free-stream value), and the relaxation constant is estimated as $K_p = \beta c(1 - \mathcal{M}^2)/L_x$, where \mathcal{M} is the maximum Mach number of the flow, L_x is the streamwise extent of the computational domain, and $\beta \approx 0.27$. This type of outflow condition will be hereafter referred to as PRCBC (pressure relaxation characteristic boundary condition). A similar approach was pursued for the case of subsonic inflow by Yoo et al. [6], who estimated the amplitude of the incoming waves according to

$$\begin{cases} \mathcal{L}_2 = K_T(T_b - T^*), \\ \mathcal{L}_3 = K_v(v_b - v^*), \\ \mathcal{L}_4 = K_w(w_b - w^*), \\ \mathcal{L}_5 = K_u(u_b - u^*), \end{cases} \quad (12)$$

with suitable prescription of the relaxation constants. This type of inflow condition will be hereafter referred to as IRCBC (inflow relaxation characteristic boundary condition).

Several variants of the NSCBC approach have been attempted. Some studies [4] have pointed to the importance of an appropriate treatment of the transverse terms to minimize numerical reflections in the case of waves radiating out of the computational domain at an angle with respect to the boundary normal, and at corners. Other [7] proposed modifications of the pressure relaxation approach to minimize the reflection of acoustic waves. Yet other studies were aimed at using the NSCBC approach to design silent inflow conditions for the simulation of subsonic turbulent flows. For instance, Guézenec and Poinso [8] proposed a simplified version of the LODI relations to stimulate vortical disturbances at a subsonic inflow, whereby the characteristic wave amplitudes are prescribed as follows

$$\mathcal{L}_2 = 0, \quad \mathcal{L}_3 = -\partial v^* / \partial t, \quad \mathcal{L}_4 = -\partial w^* / \partial t, \quad \mathcal{L}_5 = -\rho c \partial u^* / \partial t, \quad (13)$$

which are derived from low-Mach number expansion of the Euler equations. The NSCBC approach has also been extended to generalized curvilinear coordinates [9].

The nonreflecting performance of numerical boundary conditions can be significantly enhanced by suitably damping the amplitude of disturbances before they hit the boundary. For that purpose, several strategies are available, which include grid stretching coupled with filtering of the flow variables [10], super-grid modeling to correct unphysical effects of domain truncation [11], and the use of sponge layers [12], whereby forcing terms are added to the governing equations to cause the flow to relax to prescribed target conditions. The latter approach has become increasingly popular in recent years for reducing the reflectivity at outflows and free boundaries, and also for exciting transition to turbulence, especially in the case of free-shear flows [13]. A thorough mathematical treatment of the sponge layer technique, as well as practical suggestions for implementation, are provided in the papers by Bodony [14] and Mani [15].

In this paper we propose a simple procedure to develop unsteady characteristic far-field boundary conditions for very general flow configurations. Disregarding for the present purposes the influence of transverse terms, we focus our attention on the treatment of the normal-to-boundary derivatives, through a modification of the basic NSCBC approach. The paper is organized as follows. In Section 2 we present the principles of our method, and in Section 3 we proceed to analyze its non-reflecting properties and its response to incoming disturbances. Numerical tests of the method are presented in Section 4, and concluding remarks are given in Section 5.

2. Formulation of the method

The method that we propose to advance the numerical solution at the computational boundary ($x = x_b$) is based on the characteristic form of the equations as given in (3), supplemented with the eigenvalue decomposition (4). Assume the set of the primitive variables, say \mathbf{v}_g , is known at the first grid point outside the computational mesh (x_g), as is frequently done when enforcing ‘hard’ numerical boundary conditions through the ghost nodes approach. This is allowed to be, in general, a function of position and time. Starting from the wave decomposition into incoming and outgoing parts,

$$\mathcal{L} = \mathcal{L}^o + \mathcal{L}^i = \Lambda_x^o \mathbf{L}_x \frac{\partial \mathbf{u}}{\partial x} + \Lambda_x^i \mathbf{L}_x \frac{\partial \mathbf{u}}{\partial x}, \quad (14)$$

our idea is to estimate the contribution of incoming waves by approximating the corresponding spatial derivatives in Eq. (3) through first-order upwind differences taken at the exterior of the computational domain (where a reference solution is

assumed to be known), while still applying the inward upwind approximation given in Eq. (6) to estimate the outgoing waves, thus obtaining

$$\mathcal{L} \approx \Lambda_x^0 D_u \mathbf{u}_b + n_x \Lambda_x^i \mathbf{L}_x \mathbf{P} \frac{\mathbf{v}_g - \mathbf{v}_b}{\Delta}, \quad (15)$$

where $\Delta = |x_b - x_g|$ is the distance from the boundary point to the ghost point. Substitution into Eq. (3) results in the semi-discretized system

$$\frac{d\mathbf{u}_b}{dt} = -\mathbf{R}_x \Lambda_x^0 D_u \mathbf{u}_b + n_x \mathbf{R}_x \Lambda_x^i \mathbf{L}_x \mathbf{P} \frac{(\mathbf{v}_b - \mathbf{v}_g)}{\Delta} + \mathbf{C}_b, \quad (16)$$

where again all matrices are evaluated at $x = x_b$. In the case that only a subset of the array of primitive variables is known outside the computational domain, or that only a subset can be used for physical considerations, Eq. (16) can still be applied, after zeroing the unknown entries of $(\mathbf{v}_g - \mathbf{v}_b)$.

Comparing Eq. 16 with 6 shows that the effect of the ansatz (15) the natural emergence of a relaxation term at the right-hand-side of the governing equations. We note that, in principle, the distance Δ is not subject to any specific constraint. However, accuracy in the approximation of the outer first spatial derivative would suggest to make it as small as possible. Furthermore, let Δ_i be the distance of the first inner point to the boundary, and let λ the local speed of any characteristic wave, the CFL stability condition dictates that the computational time step should satisfy $\Delta t \approx \Delta_i / \lambda$. Since the time constant associated with the relaxation term is $\tau \approx \Delta / \lambda$, it follows that, to avoid stiffness in its numerical approximation, $\tau \gtrsim \Delta t$, which implies $\Delta \gtrsim \Delta_i$. Hence, the natural choice $\Delta = \Delta_i$ follows as a good compromise between accuracy and stability.

It is noteworthy at this stage to highlight similarities and differences with previous approaches based on characteristic relaxation. In the case of a subsonic outflow, Eq. (15) yields the following estimate for the incoming wave amplitudes (assuming $n_x = 1$, i.e. the outflow is the right boundary)

$$\mathcal{L}^i = \Delta^{-1} [(u_b - c_b)((p_g - p_b) - \rho_b c_b(u_g - u_b)), 0, 0, 0, 0]^T, \quad (17)$$

which highlights a forcing term on the incoming acoustic wave, associated with deviations of the pressure and the normal-to-boundary velocity component from the reference state. This type of relaxation may be inappropriate in cases such as the outflow boundary in the wake of a bluff body, which is discussed in detail in Section 4.5. In such cases, since the velocity deficit persists well downstream of the body, relaxation should be performed on pressure only, and Eq. (17) would yield

$$\mathcal{L}_1 = c_b (1 - M_b) \frac{p_b - p_g}{\Delta}, \quad (18)$$

which is structurally similar to the PRCBC approach given in Eq. (11), except for the different value of the relaxation constant. Except for the minor difference in the Mach number dependent factor, also recalling that in the treatment of [5] \mathcal{M} is a constant, whereas here $M_b (= u_b/c_b)$ may change from point to point, one will notice that the restoring force is proportional to β/L_x in Eq. (11), whereas it is proportional to $1/\Delta$ in (18), which shows that here it is typically stronger than the theoretical optimum. The practical effectiveness of our approach will be documented through numerical simulations. Similarly, the method can be specialized to the case of a subsonic inlet, which will highlight qualitative similarities with the relaxation procedure of Yoo et al. [6], as given in Eq. (12).

Despite formal similarities with previous relaxation methods, in our approach the form of the relaxation term is a natural consequence of the characteristic decomposition, and the relaxation constant only depends on the local mesh spacing and flow properties. Furthermore, the present method implies de-coupled relaxation of each characteristic field. This is easily seen by re-casting the system (16) in terms of the characteristic variables given in Eq. (9)

$$\frac{d\mathbf{w}_b}{dt} = -\Lambda_x^0 D_u \mathbf{w}_b + n_x \Lambda_x^i \mathbf{L}_x \mathbf{P} \frac{(\mathbf{v}_b - \mathbf{v}_g)}{\Delta} + \mathbf{L}_{xb} \mathbf{C}_b, \quad (19)$$

whence, assuming small deviations from the reference condition at the boundary, i.e. $\mathbf{v}_b \approx \mathbf{v}_g$, one obtains

$$\frac{d\mathbf{w}_b}{dt} = -\Lambda_x^0 D_u \mathbf{w}_b + n_x \Lambda_x^i \frac{(\mathbf{w}_b - \mathbf{w}_g)}{\Delta} + \mathbf{L}_{xb} \mathbf{C}_b, \quad (20)$$

where $\mathbf{w}_{b,g} \equiv \mathbf{L}_x \mathbf{P} \mathbf{v}_{b,g}$. Eq. (20) implies that, in the case of small perturbations with respect to a uniform state, the reflection coefficient of outgoing waves is identically zero, whereas perturbations conveyed by incoming waves are exponentially damped in time, since the relaxation constant associated with the ℓ th characteristic field is $n_x \lambda_\ell^i / \Delta \leq 0$. This is in contrast with previous relaxation-based techniques, which subtend coupled relaxation of the characteristic fields, as clear from Eqs. (11), (12). This is also important because the absence of reflections implies well-posedness of the boundary conditions, at least in the one-dimensional, linearized setting [16]. We finally note that the present procedure is easily applicable to the case that an asymptotic (non-uniform) solution is known for the far flow field, in which case the target primitive vector \mathbf{v}_g stands for the local asymptotic state near the boundary.

The proposed characteristic relaxation method also bears resemblance with the widely used summation by parts-simultaneous approximation term (SBP-SAT) technique, developed for the scalar case by Carpenter et al. [17], and extended thereafter to the three-dimensional Navier–Stokes equations by Svård et al. [18], and to handle wall boundary conditions [19]. The

main idea of the SAT approach is to add a relaxation term to the discretized equations at some nodes near the boundary, in such a way as to satisfy an energy inequality, thus guaranteeing the time stability of the numerical algorithm. However, while the form of the relaxation term is similar, there are important differences between SAT and the present method, which are highlighted in the Appendix. First, in the present approach, the relaxation term stems directly from the discretization process, and it is not an addition needed for stabilization purposes. Second, the present method only requires modification at the boundary nodes, and thus modifications to existing algorithms are local in nature. Third, while the present method does not guarantee strict energy stability as it spoils the SBP structure of the discrete derivative operator, it can still be proven to yield bounded energy in the case of central second-order difference operators, and, for more complex discretizations, it is found to be robust in practice. As shown by Bodony [20], the effectiveness of the SBP-SAT technique is comparable to that of classical characteristic-based methods, to which we compare the performance of the proposed method in Section 4.

3. Analysis of the method

The performance of the proposed generalized relaxation characteristic boundary conditions (hereafter referred to as GRCBC method), as expressed by Eq. (16) is analyzed next, following Polifke et al. [7]. To characterize the behavior of different numerical boundary conditions we consider the simplified set of one-dimensional acoustic equations derived from (10) by setting to zero the strength of the entropy and vorticity waves, and linearizing about an underlying uniform state (the associated properties are denoted with an overbar), under the assumption that fluctuations thereof (the prime symbol is suppressed) are small,

$$\frac{\partial u}{\partial t} + \frac{1}{2\bar{\rho}\bar{c}}(\mathcal{L}_5 - \mathcal{L}_1) = 0, \quad (21)$$

$$\frac{\partial p}{\partial t} + \frac{1}{2}(\mathcal{L}_5 + \mathcal{L}_1) = 0, \quad (22)$$

where, in the case of subsonic mean flow, field 1 ($\lambda_1 = \bar{u} - \bar{c}$, $w_1 = -\bar{\rho}\bar{c}u + p$) carries left-running acoustic waves, and field 5 ($\lambda_5 = \bar{u} + \bar{c}$, $w_5 = \bar{\rho}\bar{c}u + p$) carries right-running acoustic waves. Fourier transforming in time Eqns. (21), (22) yields

$$\hat{u} - \frac{1}{2\bar{\rho}\bar{c}}(\hat{w}_5 - \hat{w}_1) = 0, \quad (23)$$

$$\hat{p} - \frac{1}{2}(\hat{w}_5 + \hat{w}_1) = 0, \quad (24)$$

where the Fourier coefficients are denoted with the caret symbol, after noticing that, since $\mathcal{L}_i = -\partial w_i / \partial t$, $\hat{\mathcal{L}}_i = i\omega \hat{w}_i$.

To quantify the nonreflecting performance of numerical boundary conditions at the outflow we define the reflection coefficient as

$$r_o(\omega) = \frac{\hat{w}_1}{\hat{w}_5}. \quad (25)$$

The PRCBC approach of Eq. (11) implies

$$\hat{w}_1 = \frac{K_p}{i\omega} \hat{p}, \quad (26)$$

which, inserted into (25), and accounting for (24) yields

$$r_o(\omega) = \frac{1}{2i\omega/K_p - 1}. \quad (27)$$

The same expression was also arrived at by Selle et al. [21], and makes it clear that pressure relaxation boundary conditions are partially reflective to acoustic waves. In the case of the GRCBC approach, the time variation of the incoming wave given by Eq. (15) is

$$\mathcal{L}_1 = \frac{\lambda_1}{h}(w_{1g} - w_1), \quad (28)$$

where w_{1g} is the nominal amplitude of the characteristic field 1 at the first exterior node (x_{N+1}). If the target field coincides with the mean flow, $w_{1g} = 0$, and the reflection coefficient is then identically zero, since $i\omega \hat{w}_1 = \lambda_1/h \hat{w}_1$ implies $\hat{w}_1 = 0$. The improvement over the PRCBC approach is clearly due to the use of characteristic-wise relaxation.

Let us consider next a subsonic inflow where a reference, generally space-and-time varying reference state $p^*(x, t)$, $u^*(x, t)$ is known, associated with an incoming acoustic wave $w_5^* = \bar{\rho}\bar{c}u^* + p^*$. The nonreflecting performance of inflow conditions can then be quantified in terms of the reflection coefficient

$$r_i(\omega) = \frac{\hat{w}_5}{\hat{w}_1}. \quad (29)$$

The IRCBC approach, as given by Eq. (12), amounts to estimating the amplitude of the incoming wave at the inflow node $x_1 = 0$ as

$$\mathcal{L}_5 = K_u(u - u^*(0, t)), \quad (30)$$

which transforms into

$$\hat{w}_5 = \frac{K_u}{i\omega}(\hat{u} - \hat{u}^*(0)). \quad (31)$$

Taking into account Eq. (23) one then obtains the amplitude of the incoming wave

$$\hat{w}_5 = \frac{\hat{w}_1}{1 - 2i\bar{\rho}\bar{c}\omega/K_u} + \frac{\hat{w}_5^*(0)}{1 - 2i\bar{\rho}\bar{c}\omega/K_u}. \quad (32)$$

Taylor expansion of its reflection coefficient

$$r_i(\omega) = \frac{1}{1 - 2i\bar{\rho}\bar{c}\omega/K_u}, \quad (33)$$

then shows that the IRCBC method is nonreflecting to left-running acoustic waves to $O(\omega)$, and its response to incoming disturbances, as quantified by the ratio $\hat{w}_5/\hat{w}_5^*(0)$, is also accurate to $O(\omega)$.

In the case of a subsonic inflow, the GRCBC formulation (16) reduces to

$$\frac{dw_5}{dt} = -\frac{\bar{u} + \bar{c}}{h}(w_5 - w_5^*(-h, t)), \quad (34)$$

which transformed to Fourier space yields

$$\hat{w}_5 = \frac{\hat{w}_5^*(-h)}{1 - iz} = \frac{\hat{w}_5^*(0)e^{-iz}}{1 - iz}, \quad (35)$$

where $z = \omega h/(\bar{u} + \bar{c})$. Eq. (35) shows that the incurred reflection error is identically zero, and Taylor expansion shows that the response to incoming disturbances is accurate to $O(\omega^2)$.

To summarize we find that, at least in a linear setting, the GRCBC method has a twofold advantage: (i) it exactly prevents the reflection of acoustic waves at computational boundaries, unlike classical relaxation procedures, since the characteristic fields are decoupled; (ii) in the presence of a time-varying reference state outside the computational domain, the method guarantees improved frequency response, being (in the case here considered of second-order interior discretization) accurate to $O(\omega^2)$, rather than $O(\omega)$.

4. Numerical tests

The GRCBC method designed in Section 2 is here applied to a series of benchmark problems, in increasing order of complexity. Whenever possible, we also present a comparison with previous characteristic-based artificial boundary condition methods. Specifically, the PRCBC and the IRCBC method are considered, with the same prescription of the relaxation constants given in the original references [3,6]. To evaluate the effect of numerical boundary conditions, the equations are discretized at interior nodes through second-order central difference formulas, which avoids any additional uncertainty associated with modification of the discrete derivative stencil near boundaries. To increase the robustness of the code (which is useful in turbulent flow computations), the convective terms are suitably split prior to being discretized, in such a way that semi-discrete conservation of the total kinetic energy is guaranteed in the limit of incompressible, inviscid flow [22], for periodic domains. Unless otherwise specified, backward discrete derivative operators (the D_u in Eq. 16) with second-order accuracy are used at the boundary nodes. All test cases, except the boundary layer simulation, are performed in two space dimensions. Viscosity is set to zero in all test cases except for the cylinder and the boundary layer flow.

4.1. Propagation of a zero-circulation, cylindrical vortex

The first test consists in the passive advection of a circular, homentropic, zero-circulation vortex, out of the computational domain. The vortex is initially centered at the origin of the coordinate system, and velocity, density and pressure are specified as follows

$$\begin{cases} \frac{u(x,y)}{u_\infty} = 1 - \frac{M_v}{M_\infty} \frac{y-y_0}{r_v} e^{(1-\hat{r}^2)/2}, \\ \frac{v(x,y)}{u_\infty} = \frac{M_v}{M_\infty} \frac{x-x_0}{r_v} e^{(1-\hat{r}^2)/2}, \\ \frac{\rho(x,y)}{\rho_\infty} = \left(1 - \frac{\gamma-1}{2} M_v^2 e^{1-\hat{r}^2}\right)^{\frac{1}{\gamma-1}}, \\ \frac{p(x,y)}{p_\infty} = \left(1 - \frac{\gamma-1}{2} M_v^2 e^{1-\hat{r}^2}\right)^{\frac{\gamma}{\gamma-1}}, \end{cases} \quad (36)$$

where r_v is the radius of the vortex core, M_v is the vortex Mach number based on the maximum vortex-induced tangential velocity (U), and the free-stream sound speed (c_∞), $M_\infty = u_\infty/c_\infty$ is the free-stream Mach number, and $\hat{r} = r/r_v$, $r^2 = x^2 + y^2$. Numerical results are shown for a mesh covering the rectangle $[-20r_v : 20r_v] \times [-10r_v : 10r_v]$, and including 512×256 grid points. Several combinations of advection velocity and vortex strength are considered, (A) $M_\infty = 0.3, M_v = 0.1$; (B) $M_\infty = 0.3, M_v = 0.4$; (C) $M_\infty = 1.2, M_v = 0.4$. The first two cases provide indications on the performance of artificial boundary conditions for subsonic flow, and case B is particularly challenging in that the streamwise velocity exhibits an inversion of sign as the vortex crosses the boundary. Case C is relatively less challenging in that waves at the inflow and the outflow all point to the same direction, being the flow supersonic throughout.

Several simulations have been performed to establish the effect of numerical boundary conditions, considering different combinations of closures on the four sides of the mesh. In the simulations labeled as NRCBC, the baseline nonreflecting closure Eq. (5) is applied on all four sides; the PRCBC simulations are performed with nonreflecting closures on all sides, except for the outflow boundary, where Eq. (11) is applied; the IRCBC simulations are performed with nonreflecting closures on all sides, except for the inflow boundary, where Eq. (12) is applied; and the GRCBC simulations are performed using the closure given in Eq. (16) on all sides, assuming that the undisturbed flow conditions hold in the whole layer of ghost nodes around the computational mesh.

Representative results are shown in Figs. 1 and 2, where we report the time evolution of the r.m.s. and maximum vertical velocity. In the figure the exact solution of the problem is also indicated as a thick solid line. As expected, the vortex-induced velocity becomes essentially zero after the vortex is convected past the right boundary, which happens at $tu_\infty/r_v \approx 20$. This is not the case for the numerical solutions, which all exhibit lack of perfect transparency, to a varying extent though. In the two subsonic cases (panels a,b) the GRCBC method exhibits improved effectiveness in the absorption of disturbances after the first numerical reflection, by about an order of magnitude compared to the other methods. The disturbances left in the

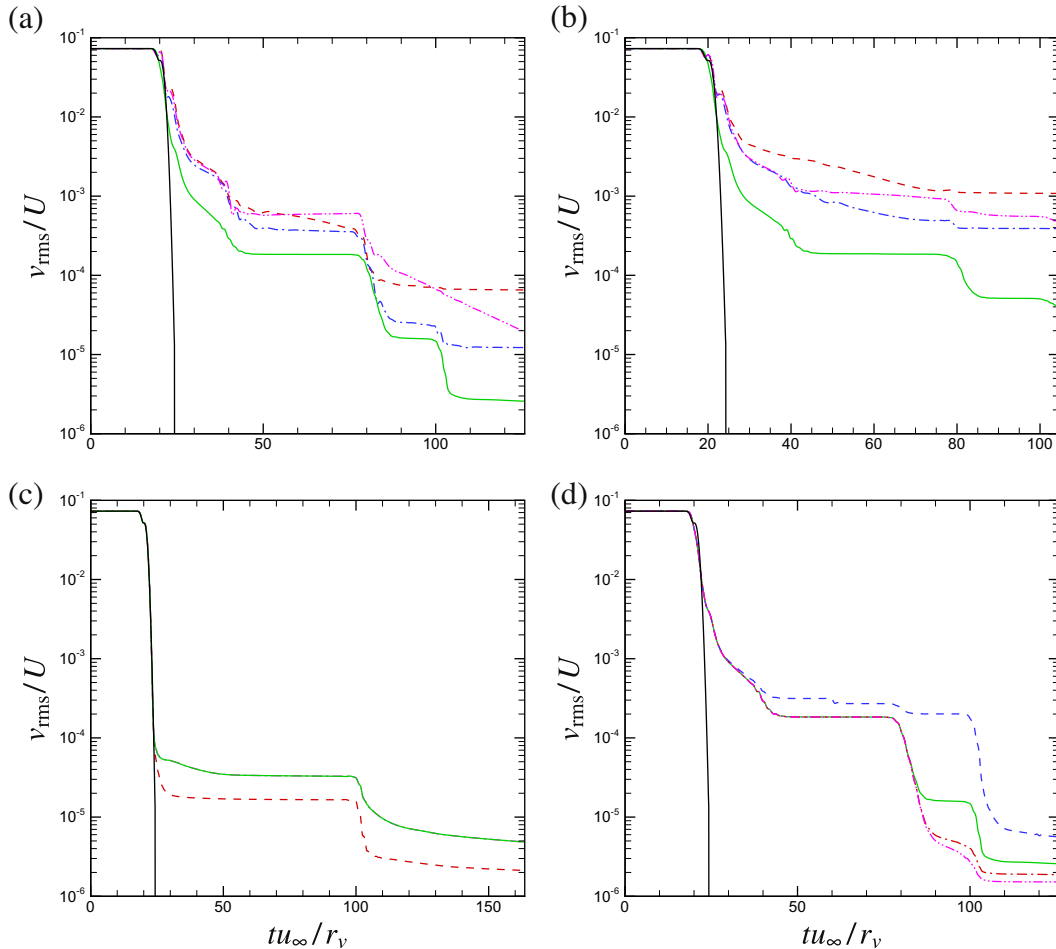


Fig. 1. Time evolution of r.m.s. vertical velocity for cylindrical vortex advection. Thick solid line: exact solution; solid line, GRCBC; dashed line, NRCBC; dot-dashed line, PRCBC; dot-dot-dashed line, IRCBC. (a), effect of boundary condition type for weak vortex in subsonic flow (test case A); (b), effect of boundary condition type for strong vortex in subsonic flow (test case B); (c), effect of boundary condition type for strong vortex in supersonic flow (test case C); (d), effect order of boundary derivative for weak vortex in subsonic flow (test case A). In panel (d) the lines correspond to closures of order from one to four (top to bottom).

computational domain are further damped in the course of successive numerical reflections. The advantage of the GRCBC method is confirmed over long times, and it is more evident in the tougher case of strong vortex (panel b). The scenario changes somewhat for the supersonic flow case (panel c), in which (perhaps not surprisingly) purely nonreflecting boundary conditions have marginally superior performance. For obvious reasons, test case C has not been computed with the PRCBC and IRCBC methods. Finally, panel (d) shows the effect of varying the order of accuracy of the backward derivative operator (D_u) in Eq. (16), for test case A. Marginally better results are obtained as the order of accuracy is increased, the improvement saturating around third order.

Further support to the validity of the GRCBC approach is provided in Fig. 3, where we show the evolution of the vorticity and pressure field in a time window about the impingement of the vortex on the right boundary. Results are only shown for the toughest flow case, namely test B. While vorticity is left free to propagate out of the domain, some spurious feedback pressure waves are observed for any numerical boundary treatment. However, the reduction in the amplitude of the reflected waves conveyed by use of GRCBC is evident.

4.2. Radiation of a pressure pulse

The second test consists in the radiation of an acoustic pulse from a Gaussian excess pressure zone. The fluid is initially at rest, and density and pressure are specified as follows

$$\begin{cases} \frac{\rho(x,y)}{\rho_\infty} = \left(1 - \frac{\gamma-1}{2} \alpha^2 e^{1-r^2}\right)^{\frac{1}{\gamma-1}}, \\ \frac{p(x,y)}{p_\infty} = \left(1 - \frac{\gamma-1}{2} \alpha^2 e^{1-r^2}\right)^{\frac{\gamma}{\gamma-1}}, \end{cases} \quad (37)$$

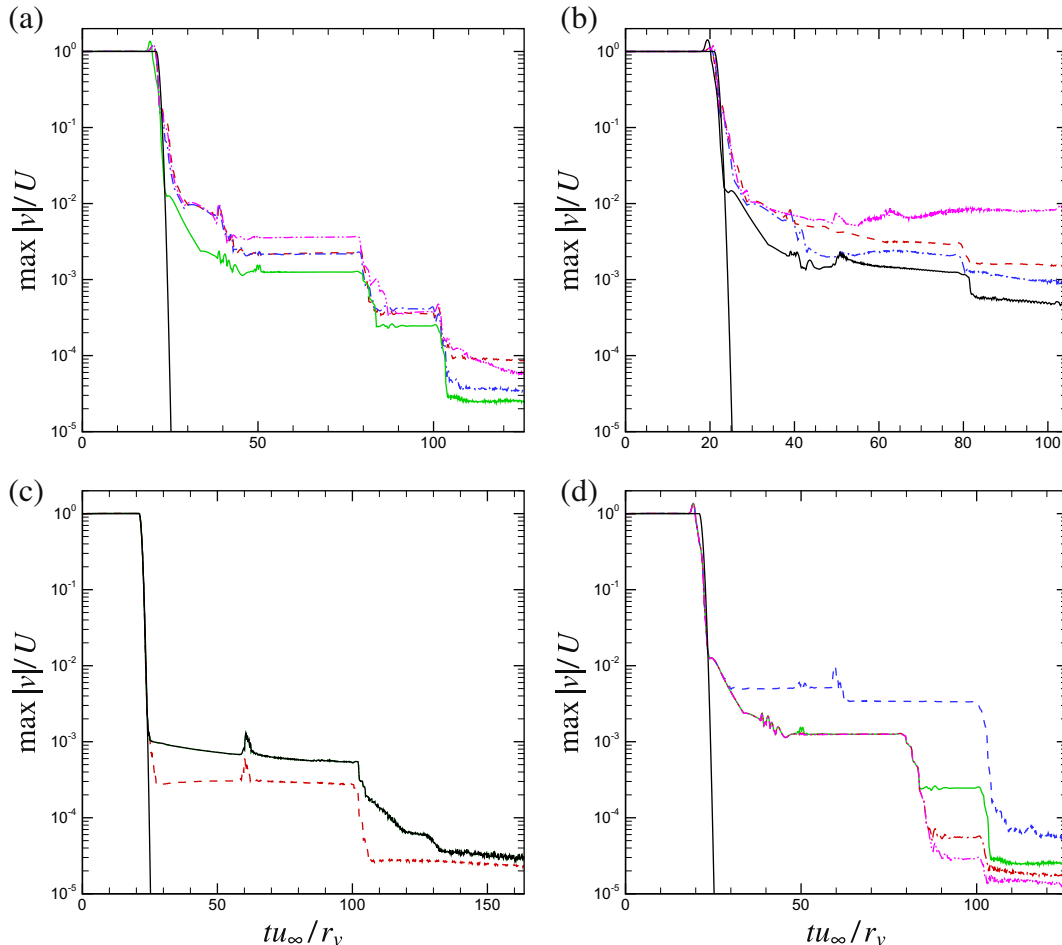


Fig. 2. Time evolution of maximum vertical velocity for cylindrical vortex advection. Thick solid line: exact solution; solid line, GRCBC; dashed line, NRCBC; dot-dashed line, PRCBC; dot-dot-dashed line, IRCBC. (a), effect of boundary condition type for weak vortex in subsonic flow (test case A); (b), effect of boundary condition type for strong vortex in subsonic flow (test case B); (c), effect of boundary condition type for strong vortex in supersonic flow (test case C); (d), effect order of boundary derivative for weak vortex in subsonic flow (test case A). In panel (d) the lines correspond to closures of order from one to four (top to bottom).

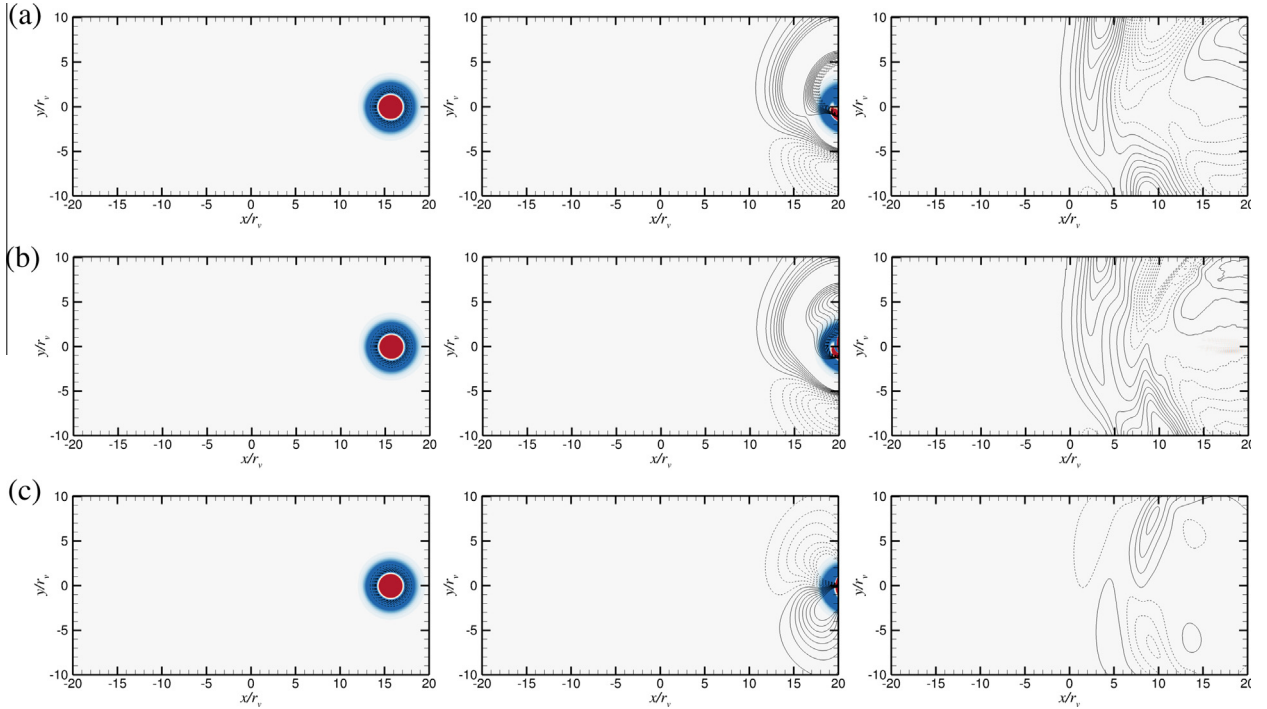


Fig. 3. Advection of cylindrical vortex with $M_\infty = 0.3, M_v = 0.4$ (test case B): pressure and vorticity contours at $tu_\infty/r_v = 10.5, 15.7, 20.9$ (left to right) obtained with (a) NRCBC; (b) PRCBC; (c) GRCBC. Vorticity contours are shown in color, from blue (negative values) to red (positive values). 16 equally-spaced pressure contours are shown ($-0.02 \leq p/p_\infty - 1 \leq 0.02$), negative values being denoted with dashed lines. (For interpretation of the references to colour in this figure caption, the reader is referred to the web version of this article.)

where $\alpha = 0.4$ is the initial strength of the pulse, and the same notation is used as for the cylindrical vortex case. Numerical results are shown for a mesh covering the interval $[-4r_v : 4r_v] \times [-4r_v : 4r_v]$, and including 64×64 grid points. The r.m.s. and maximum pressure are shown in Fig. 4 as a function of time. The exact solution, shown in the figure as a thick solid line, indicates fast decay of pressure disturbances after the pulse hits the boundary, which happens at $tc_\infty/r_v \approx 3$. The exact behavior is reproduced by both the nonreflecting and the generalized relaxation method up to $tc_\infty/r_v \approx 6$, after which the GRCBC method exhibits stronger damping of the disturbances, even though no substantial improvement is observed.

What is more interesting to observe though is that the method can also work under flow conditions for which straightforward application of the standard nonreflecting approach is prevented. For that purpose, we consider the same pressure pulse test case in a rotating reference frame. We then assume that the initial velocity field is given by

$$\begin{cases} u(x, y)/c_\infty = -\Omega y, \\ v(x, y)/c_\infty = \Omega x, \end{cases} \quad (38)$$

with $\Omega = 0.1\sqrt{\gamma}c_\infty/r_v$, and add body forces to the right-hand-side of the Navier–Stokes equations to account for centrifugal and Coriolis force effects. The GRCBC method is enforced by advancing at all mesh boundaries Eq. (16), the target values of the velocity components being given by (38), and pressure and density being equal to the free-stream values. As testified by Fig. 5, the mean rotating flow is extremely well maintained by the relaxation boundary conditions even over very long times, the streamlines remaining closed with high degree of accuracy. Regarding the nonreflecting capability of the method, Fig. 4 shows similar performance compared to the case of zero mean flow at early times, even though a tendency for small disturbances to attain a non-zero asymptotic state is observed in the rotating frame. Overall, we believe that this is a convincing proof of the capability of the method to adapt itself to flow cases with complex far-field conditions, one natural instance being the prediction of flows around rotating objects is the co-rotating reference frame.

4.3. Injection of a zero-circulation, cylindrical vortex

To test the suitability of the method for the soft enforcement of inflow vortical disturbances without inducing spurious reflections, we again consider the vortex propagation test case discussed in Section 4.1, but in a shifted computational domain $[5r_v : 45r_v] \times [-10r_v : 10r_v]$, covered with 512×256 grid points. In this case the vortex initially lies outside the computational domain, and non-homogeneous inflow boundary conditions are necessary to stimulate its injection. The same test conditions of [8] have been initially considered, which correspond to $M_\infty = 0.288, M_v = 0.086$, with equivalent resolution in

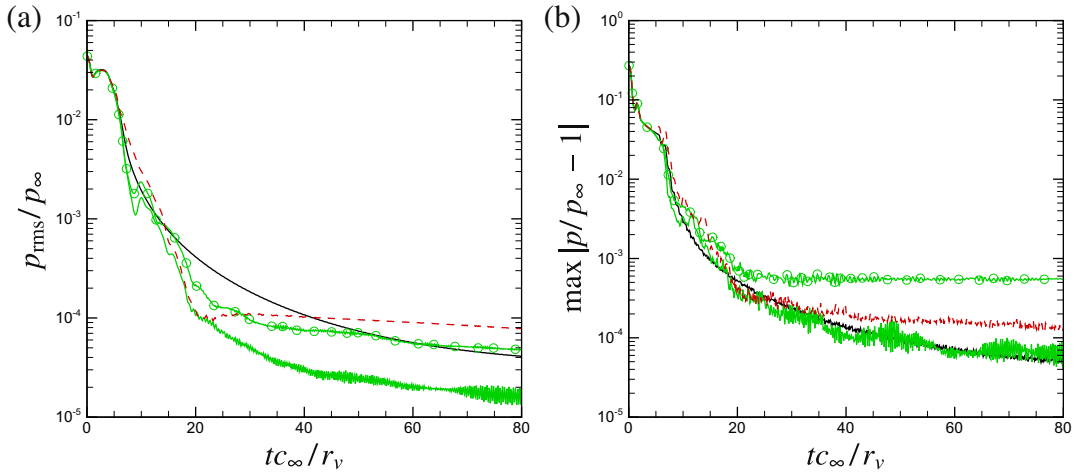


Fig. 4. Pressure pulse radiation: time evolution of r.m.s. (a) and maximum pressure fluctuations (b). Thick solid line: exact solution; solid line, GRCBC; dashed line, NRCBC; circles, GRCBC in rotating reference frame.

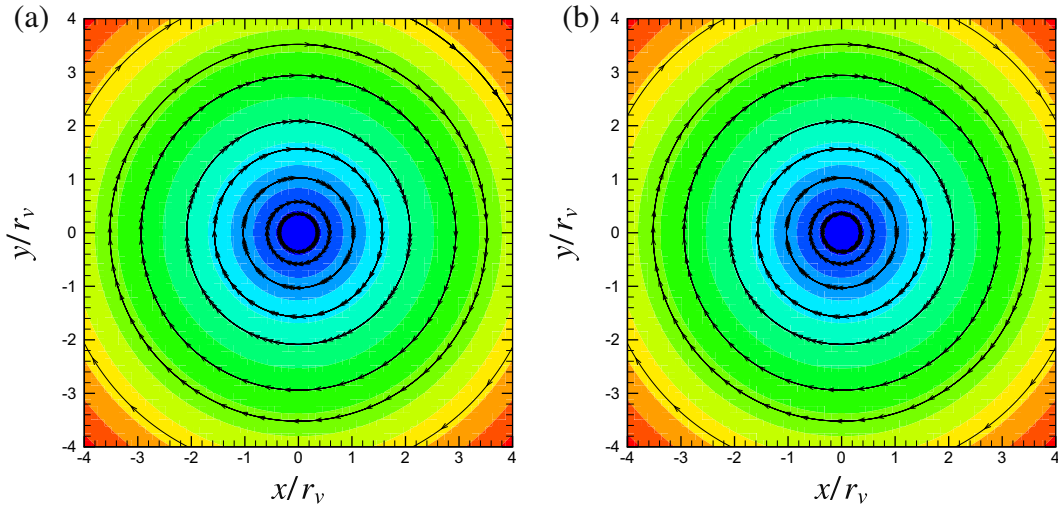


Fig. 5. Pressure pulse radiation in a rotating reference frame: instantaneous streamtraces and contours of velocity modulus at the beginning (a) and at the end $tc_\infty/r_v = 80$ of the simulation (b).

terms of grid points per vortex radius. The same test case was also repeated for a stronger vortex with $M_v = 0.4$, which features inversion of the streamwise velocity as the vortex enters the domain. The GRCBC approach is here used to numerically enforce boundary conditions at the inflow (the left side of the domain), using the exact solution of the problem (as given in Eq. 36, duly translated in time) as a time-varying target state. The results of this test case are presented in Figs. 6, 7, and compared to the exact solution of the problem. The time history of pressure and vertical velocity at the first grid node, shown in Fig. 6, clearly indicate that the numerical boundary conditions are capable of injecting the vortex without significant distortions, the numerical solution being nearly indistinguishable from the exact one (relative errors are less than 1%). Apparently, the behavior is significantly better than observed by Guézennec and Poinso [8], who reported underestimation of the pressure drop within the vortex core by 10–15%, when the set of inflow boundary conditions given in Eq. (13) is used. The quality of the GRCBC approach can also be appreciated from Fig. 7, where we show the time history of the r.m.s. and maximum vertical velocity. The numerical solution is found to reproduce extremely well the rise and saturation of the vortex strength as it convects across and past the inflow station. As previously observed when commenting the baseline convecting vortex simulations, suppression of the disturbances by over two orders of magnitude is observed after ($tu_\infty/r_v \gtrsim 45$) the vortex exits the right side of the flow domain. Such drop is not observed when hard inflow boundary conditions are specified at the inflow, i.e. when the values of all primitive values are explicitly imposed at the inflow ghost nodes to compute the interior derivatives, because of the onset of undamped saw-tooth waves, as indicated by the much higher

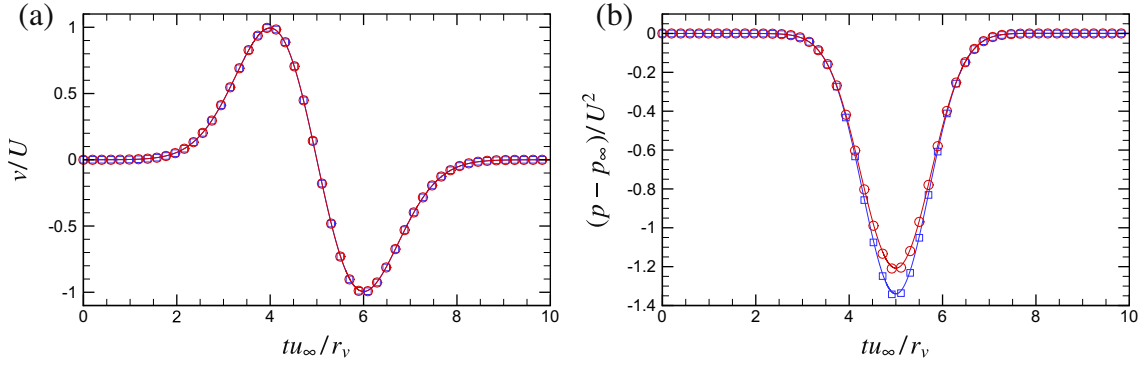


Fig. 6. Injection of cylindrical vortex: time evolution of vertical velocity (a) and pressure (b) at the inflow ($x = 5r_v$, $y = 0$). Solid lines: GRCBC. Symbols denote the exact solution for $M_v = 0.086$ (squares) and $M_v = 0.4$ (circles).

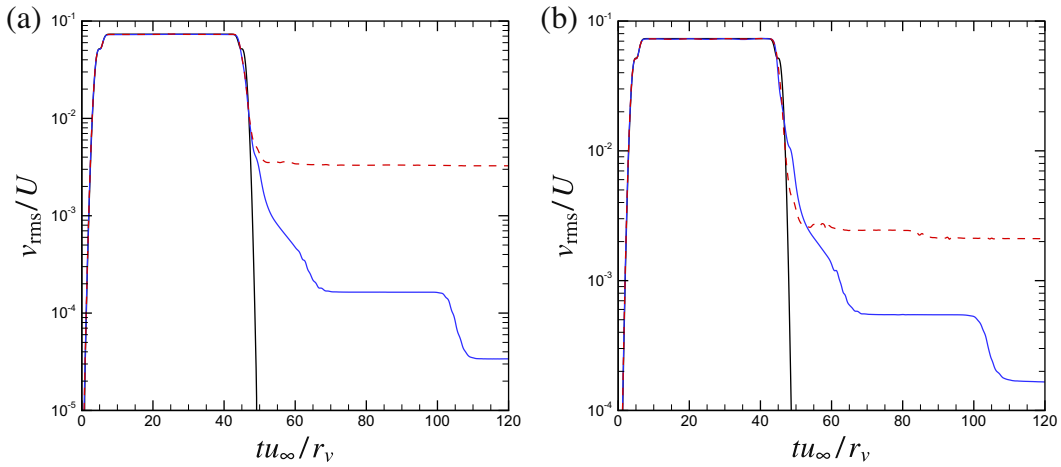


Fig. 7. Injection of cylindrical vortex with $M_v = 0.086$ (left), and $M_v = 0.4$ (right): time evolution of r.m.s. vertical velocity fluctuations. Thick solid line: exact solution; solid line, GRCBC; dashed line, hard inflow boundary conditions.

level of disturbances after the vortex leaves the computational box, which are clearly visible in flow visualizations (not shown).

4.4. Interaction of spatially decaying turbulence with harmonic acoustic wave

This test case replicates that proposed by Guézenne and Poinot [8] to qualify inlet boundary conditions for the simulation of acoustic instabilities in combustion chambers. The main flow consists of a uniform stream with Mach number $M_0 = 0.3$, with superposed synthetic velocity fluctuation that reproduce an isotropic two-dimensional turbulence state. For that purpose, an ensemble of Gaussian vortices of the type given in Eq. (36) is stimulated at the inlet, with random spatial distribution, and with fixed radius (say, r_v) and strength (this is at difference with Guézenne and Poinot [8], who also prescribed a Gaussian random distribution for the vortex radii and strengths), in such a way that the inlet turbulent Mach number is $M_t = (u_i^2)^{1/2}/c_0 = 0.04$. For practical implementation purposes, the effect of each Gaussian vortex is superposed at the inlet, and the resulting density, velocity and pressure fields are used to form the vector of the target variables in Eq. (16). A left-running sinusoidal acoustic wave is also excited at the outlet of the computational domain, $x = L_x$, with pressure

$$p_{ac}(L_x, y, t) = \alpha p_0 \sin(2\pi f_0 t), \quad (39)$$

where $\alpha = 0.01$, $f_0 = 3c_0/(4L_x)$, and c_0 is the speed of sound of the undisturbed medium, to mimic flow cases in which turbulence is injected in a resonant flow. This test case is particularly challenging for inlet boundary conditions, as a good method must have the capability to inject vorticity perturbations while allowing acoustic disturbances to exit the domain. In particular, while a good nonreflecting method yields a flat distribution of the root-mean-square pressure, since the hydrodynamic pressure fluctuations are much smaller for this test case, reflective boundary conditions lead to the development of a stationary longitudinal mode, whose variance is given by Guézenne and Poinot [8]

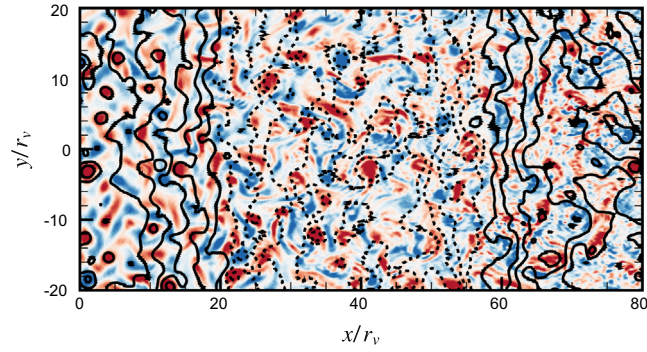


Fig. 8. Interaction of turbulence with acoustic wave. Flooded contours correspond to zones with clockwise vorticity (blue) and counter-clockwise vorticity (red). Lines indicate contours of pressure fluctuations from $p'/p_0 = -0.01$ to 0.01 , the dashed lines denoting negative values. (For interpretation of the references to color in this figure legend, the reader is referred to the web version of this article.)

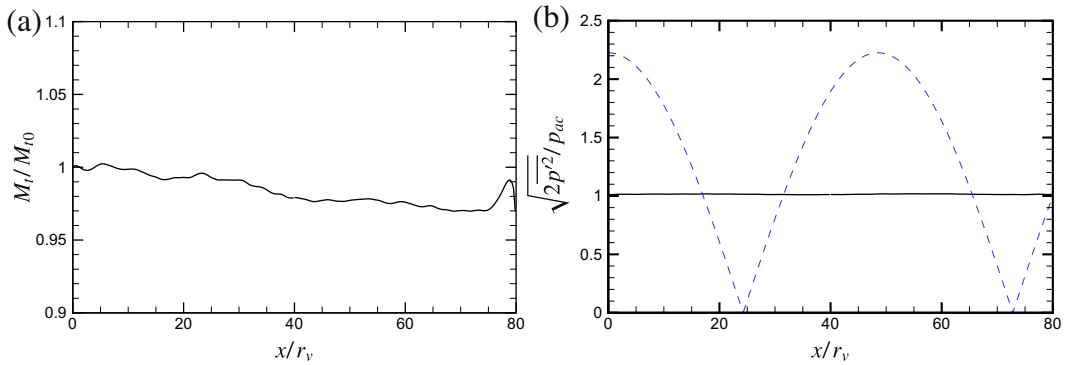


Fig. 9. Interaction of turbulence with acoustic wave: streamwise evolution of turbulent Mach number (a), and root-mean-square pressure fluctuations (b). The dashed line in panel (b) denotes the spurious stationary mode as from Eq. (40).

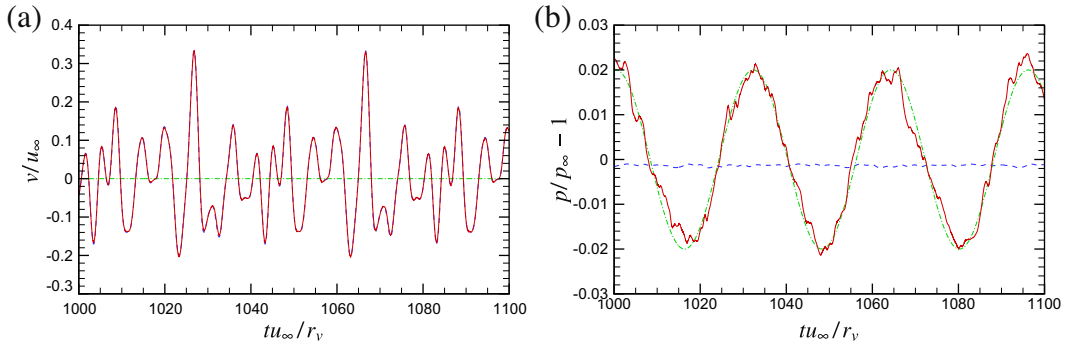


Fig. 10. Interaction of turbulence with acoustic wave: time evolution of vertical velocity (a) and pressure (b) at the inflow ($x = 0$, $y = 0$). Solid line: numerical solution; dashed line, contribution of incoming synthetic turbulence; dot-dashed line, contribution of upstream-traveling acoustic wave.

$$\overline{p'^2}(x) = p_\omega(x)p_\omega^*(x)/2, \quad p_\omega(x) = \alpha p_0 \frac{e^{i\beta_+ x} + e^{i\beta_- x}}{e^{i\beta_+ L_x} + e^{i\beta_- L_x}}, \quad (40)$$

where the asterisk denotes the complex conjugate, and $\beta_\pm = 2\pi f_0/(1 \pm M_0)c_0$.

An instantaneous snapshot of the computed flow field is depicted in Fig. 8, where we show contours of vorticity in color, with superposed contours of pressure. The figure well highlights the feeding of quasi-circular vortices at the inflow (left) boundary, which then develop downstream into filamentary structures. Some loss or resolution may be noticed toward the outflow boundary, which is due to the use of an energy-consistent numerical discretization at zero physical viscosity. The distributions of the turbulent Mach number and of the amplitude of pressure fluctuations, averaged in time and in

the y direction, are shown in Fig. 9. Panel (a) of the figure confirms that the turbulence kinetic energy is approximately conserved as moving in the downstream direction, and it is very little affected by the acoustic wave, since the associated velocity fluctuations are much smaller than for the hydrodynamic field. Panel (b) shows that, as expected for good nonreflecting boundary conditions, the fluctuating pressure amplitude is nearly constant throughout the flow domain. For reference, in the figure we also show the (incorrect) behavior that would be obtained for an acoustically perfectly reflecting inflow condition. In Fig. 10 we show the time history of pressure and vertical velocity at the inflow station, compared with those carried by the incoming turbulent flow, and with the upstream-traveling acoustic wave. The figure clearly indicates that the GRCBC method is capable of tracking with great precision the velocity disturbances fed into the computational domain. At the same time, the reference acoustic pressure wave is accurately tracked, with obvious fluctuations around the reference trend caused by the incoming disturbances. We thus conclude that our method qualifies for application to problems of acoustic-induced combustion instabilities.

4.5. Numerical simulation of laminar flow past a circular cylinder

The laminar flow past a circular cylinder is simulated at $M_\infty = 0.1$, $Re_D = 200$ (where $D = 2R$ is the cylinder diameter) to establish the effectiveness of numerical outflow boundary treatments for flows past bluff bodies. Under these flow conditions, vortices are periodically shed in the cylinder wake, and preventing spurious reflection of pressure waves from the outflow is a challenging task for numerical boundary conditions. As mentioned in Section 2, the velocity deficit in the wake of bluff bodies persists well downstream of the body, being slowly re-equilibrated through molecular and turbulent diffusion. On the other hand, pressure is quickly equilibrated, and it is uniform across the body wake, to leading order. As a consequence, when the outflow boundary is not sufficiently far from the body, it is inappropriate to perform characteristic

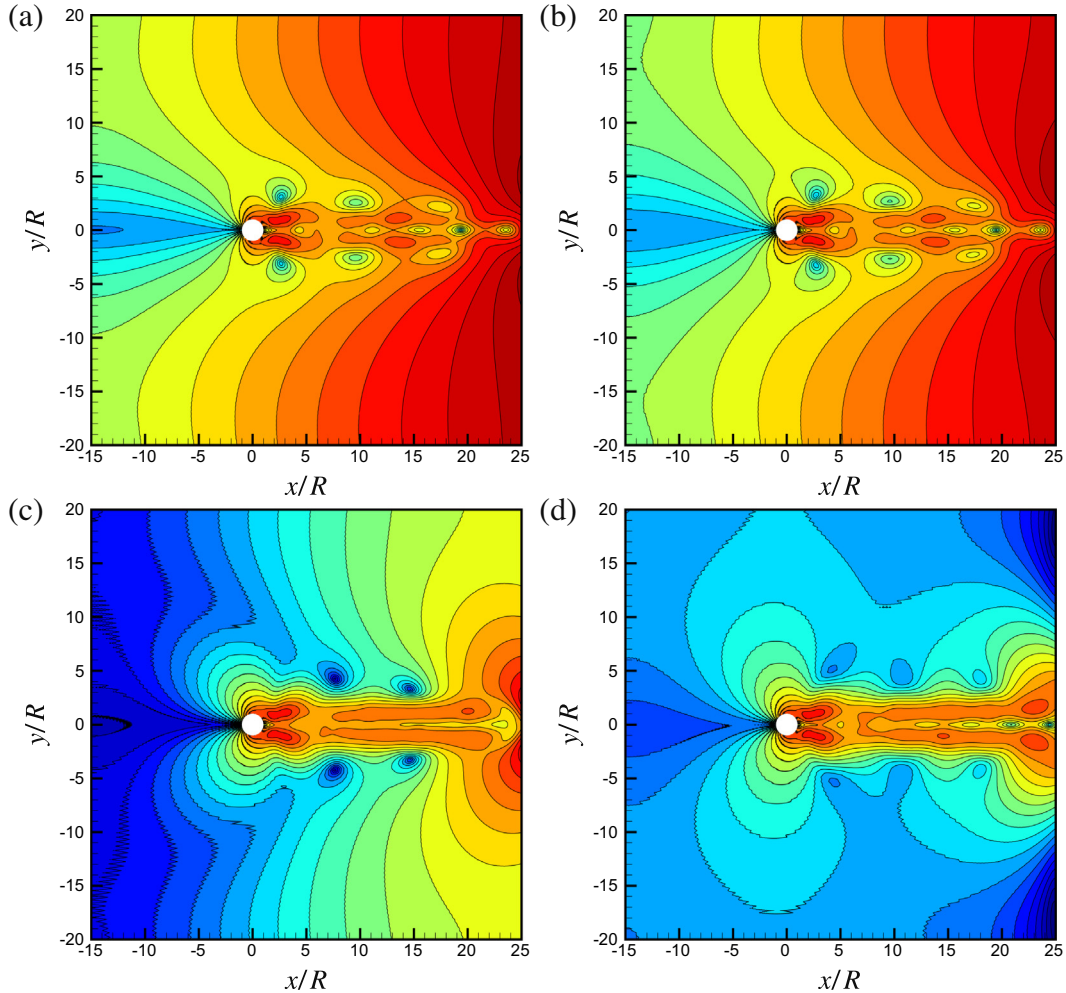


Fig. 11. Flow past circular cylinder at $M_\infty = 0.1$, $Re_D = 200$: r.m.s. pressure fluctuations ($\overline{p'^2}^{1/2}/p_\infty$). 24 contour levels are shown from 10^{-5} to 10^{-2} in logarithmic scale, from blue to red. (a) NRCBC; (b) PRCBC; (c) GRCBC; (d) GRCBC with pressure-based relaxation. (For interpretation of the references to color in this figure legend, the reader is referred to the web version of this article.)

Table 1Summary of parameters for DNS study. Mesh spacings are given in wall units taken at the station where $Re_\theta = 1000$.

M_∞	Re_θ	Δx^+	Δy^+	Δz^+	N_x	N_y	N_z
0.3	365–1105	6.00	0.75–5	5.36	2560	201	288

relaxation based on the full vectors set of the primitive variables. Considering the reduced target vector $(0, 0, 0, 0, p_\infty)$, the formulation (18) is arrived at, which we refer to here as pressure-based characteristic relaxation. As previously noted, this approach is similar to the PRCBC treatment of Rudy and Strikwerda [5], as from Eq. (11), except for the different value of the relaxation constant. The numerical tests are performed in a rectangular computational domain $[-15R : 25R] \times [-20R : 20R]$, covered with 384×256 grid points. The mesh is stretched in both coordinate directions, and the cylinder is resolved with about 30 points per cylinder radius. The circular geometry is handled on the Cartesian mesh by means of the immersed boundary method through a direct forcing approach [23]. All the rest of the computational set-up being identical, we have considered the effect of varying the numerical boundary conditions at the right side of the computational domain. The calculations have been time advanced over a sufficient time span to achieve statistical steadiness, and the flow statistics have been collected over several tens of shedding periods. Contours of the resulting root-mean-square pressure fluctuations are shown in Fig. 11. In all cases, substantial reflections from the outflow boundary are observed, associated with spurious increase of the pressure fluctuation amplitude. The amplitude of the reflected waves in the case of the NRCBC (panel a) is such to overshadow the radiated acoustic pressure, which is expected to have an essentially dipolar directivity pattern [24]. Conventional pressure relaxation based on the PRCBC approach (panel b) is not sufficient to significantly limit the amount of numerical reflection, compared to NRCBC. The dipolar directivity pattern of pressure is only recovered when the GRCBC are used. In this case, clear advantage is observed in the reducing the intensity of numerical reflections at the outlet when pressure-based characteristic relaxation is used (panel d).

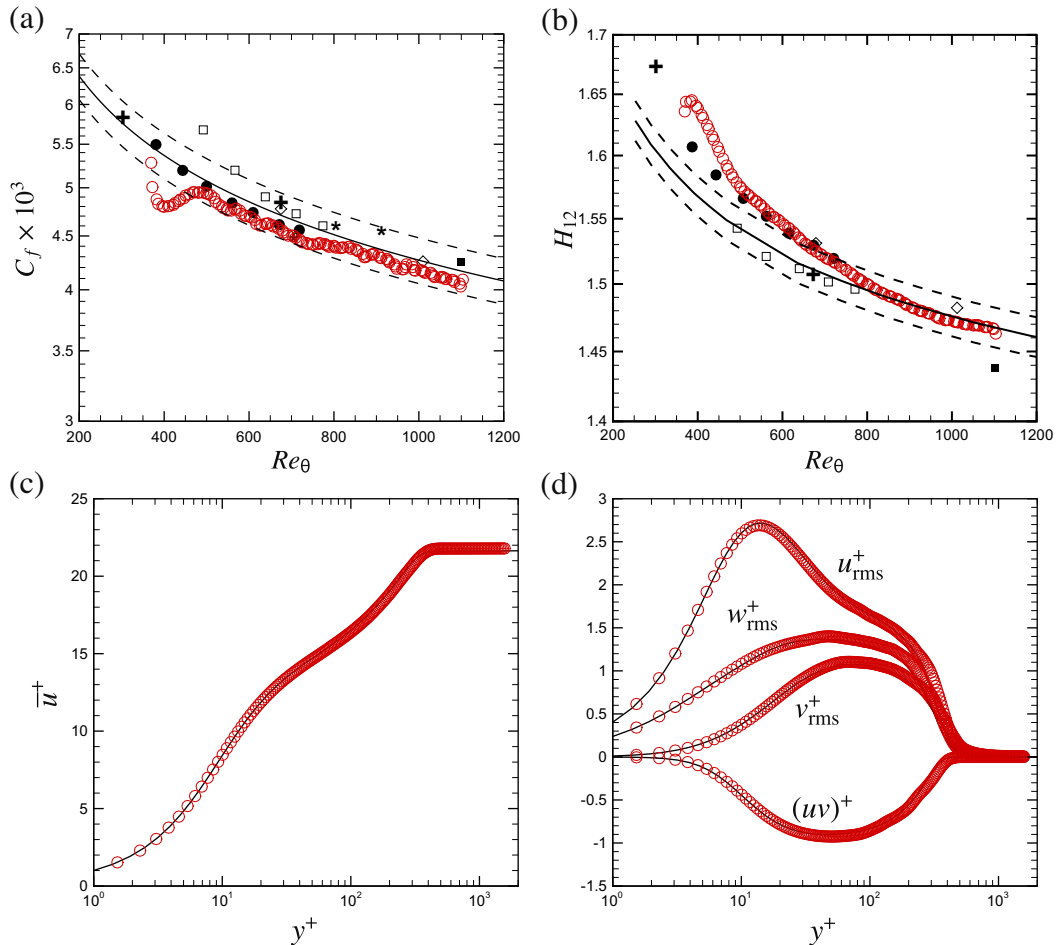


Fig. 12. Direct numerical simulation of low-speed turbulent boundary layer: (a) skin friction coefficient; (b) boundary layer shape factor, $H_{12} = \delta^*/\theta$; (c) mean velocity profile in wall units; (d) Reynolds stress components in wall units. Circles denote results from the present simulation. Other symbols: + [25], • [26], □ [27], ■ [28], ◇, ★ [30]. The solid lines in panels (c), (d) denote data from [29], at $Re_\theta = 1000$.

4.6. Direct numerical simulation of subsonic turbulent boundary layer

Apparently, the method here discussed does not suffer from the shortcomings of the vortex injection method presented by Guézennec and Poinot [8], and it does not require information on the time derivatives of the flow variables. This is especially important when the target flow is not as simple as that presented above, or it is only known numerically. This is for instance the case of the recycling/rescaling method [31], which is widely used for the enforcement of inflow boundary conditions in DNS/LES of spatially evolving wall-bounded flows. In that approach the instantaneous values of the primitive variables are collected at a given streamwise station, and are re-injected (upon suitable rescaling to account for boundary layer growth) at the inflow of the computational domain. While hard (direct) enforcement is effective in the case of strictly incompressible flow, we have found that in subsonic flow simulations it leads to severe saw-tooth oscillations of pressure, in the case that no extra numerical diffusion is explicitly added, the obvious reason being lack of nonreflectivity to upstream-traveling acoustic waves. Our goal is then to test the effectiveness of the GRCBC method for the soft implementation of the recycling/rescaling technique in subsonic flow. The implementation of the GRCBC method requires that at each time instant only one slice of data is collected at the recycling station, to form the target vector of primitive variables in Eq. (6), upon rescaling. This allows for minimization of data exchange in the case of parallel implementation, which is extremely useful to maintain computational efficiency in large-scale computations.

A spatially developing turbulent boundary layer in zero pressure gradient is simulated at $M_\infty = 0.3$, using the same method developed by Pirozzoli and Bernardini [32] for supersonic flows, with the only modification of the inflow boundary conditions. The simulation spans the range of momentum thickness Reynolds number, $Re_\theta = \rho_\infty u_\infty \theta / \mu_w$, up to about 1100, as given in Table 1. The calculation has been performed in a long domain extending for $L_x = 106 \delta_{in}$, $L_y = 10.6 \delta_{in}$, $L_z = 10.6 \delta_{in}$ in the streamwise (x), wall-normal (y) and spanwise (z) directions, δ_{in} being the 99% boundary layer thickness at the inflow station. The recycling station is set at $x_{rec} \approx 50 \delta_{in}$, which is enough to remove any possible phase locking with the disturbances re-injected at the inflow. As seen in Table 1, the mesh resolution is comparable to that of previous incompressible direct numerical simulations.

The evolution of the global flow properties (skin friction and shape factor) is shown in Fig. 12, as a function of the local momentum thickness Reynolds number. This type of representation is useful in that it conveys information on the (lack of) achievement of an equilibrium state of the simulated boundary layer [29]. Overall, the present data very well follow the trends found in previous incompressible simulations, for $Re_\theta \gtrsim 500$, which corresponds to a distance from the inflow $x/\delta_{in} \gtrsim 15$. This distance amounts to the typically quoted entry length for numerical simulations using Lund's recycling method. The velocity statistics at a station where $Re_\theta = 1000$ are shown in panels (c), (d) of Fig. 12. Again, excellent agreement of statistics up to second order is observed with the reference, strictly incompressible data of Schlatter and Örlü [29], which further supports the capability of the numerical method to generate a properly developed turbulent boundary layer.

5. Conclusions

A simple and general method for prescribing artificial boundary conditions for unsteady compressible flow solvers has been presented, which relies on one-dimensional characteristic decomposition of the governing equations at the computational boundaries. As shown in Eq. (16), the governing equations at the boundary nodes are cast in characteristic form, and, while the outgoing waves are directly approximated through inward discrete derivatives (as also in the basic NSCBC approach), the incoming waves are estimated based on the assumption that reference values of the primitive variables are known at the first (ghost) point at the exterior of the computational box. Thus, the space derivatives involved in the expression of the characteristic wave amplitudes are approximated through one-sided outward finite-difference approximations. This intuitive approach leads to a formulation which is similar to earlier relaxation-based techniques designed for subsonic outflows [3] and inflows [6], and it bears resemblance with the SBP-SAT approach [17]. The present method, however, has a twofold advantage: (i) it does not require suitably tuned relaxation constants; (ii) the relaxation is inherently characteristic-wise. As shown in Section 2, item (ii) implies that the method is exactly nonreflecting for outgoing one-dimensional acoustic waves, which is not that case when relaxation is performed based on the knowledge of pressure only. Furthermore, we have been able to prove that the method has better frequency response to incoming disturbances than other artificial inflow methods [6,8], as confirmed by numerical simulations. As such, the GRCBC method here presented is a good candidate for flow cases in which turbulence must be injected into the computational domain through an inflow plane, especially if the interest is in the prediction of the far-field sound, which must not be contaminated by numerical noise from the inflow. Numerical tests have shown success of the method in silently injecting compressible vortices, and in yielding the correct scaling laws for a subsonic turbulent boundary layer through a modification of the recycling/rescaling procedure, originally designed for strictly incompressible flow. The GRCBC method also delivers good nonreflecting performance in the case that the far field is not trivial, as for flows in rotating reference frames. For one such case, the method is proved to preserve the mean rotary velocity field with excellent accuracy, while allowing outgoing disturbances to radiate away from the computational domain. Good performance is also found for cases of relevance for the study of acoustic combustion instabilities, as the method is capable of injecting turbulence at the inflow, while still allowing feedback acoustic waves to radiate back upstream. Some caution should be exercised when dealing with flows past bluff bodies, in which case we have found that the use of a reduced target vector state which only includes pressure yields reduced reflection over full relaxation. Other

advantages of the method include avoiding the need to compute time derivatives of the target flow as in the LODI approach [8], which may be rather cumbersome from a practical standpoint, especially when the inflow data is provided synchronously with the interior calculation, as in the recycling/rescaling method. As any method based on characteristic decomposition, the GRBC method can also be easily coupled with a sponge layer to augment its performance, if needed. Straightforward extensions of the method might be the inclusion of relaxation terms for the transverse derivative contributions (as done by Lodato et al. [4]), and implementation in curvilinear coordinates, following the approach of [9].

Appendix A. Relation with the SBP-SAT technique and energy stability

The summation-by-parts/simultaneous approximation terms (SBP-SAT) technique guarantees stability of finite-difference discretizations of conservation laws in the presence of boundaries through the discrete enforcement of an energy inequality, as first proposed by Carpenter et al. [17]. To discuss similarities and differences with the proposed GRBC approach, we present here a short description of the SBP-SAT method, limited to the case of explicit finite-difference operators. A more complete presentation is provided in the original reference. The first step to develop energy-stable boundary closures is to introduce discrete derivative operators (say D) which satisfy the summation-by-parts (SBP) property. Let u, v be any two vectors of grid unknowns with N components, the $N \times N$ matrix D is said to be SBP if it satisfies the property

$$\langle u, Dv \rangle = -\langle Du, v \rangle + u_N v_N - u_1 v_1, \quad (41)$$

where the inner product is defined through a symmetric (possibly diagonal) matrix H ,

$$\langle u, v \rangle = \sum_{i=1}^N u_i H_{ij} v_j. \quad (42)$$

Eq. (41) is the discrete counterpart of the integration by parts property, and it is the key to obtain discrete energy estimates. Application of D to semi-discretize the linear advection equation (with advection speed $\lambda > 0$) yields

$$u_t + \lambda Du = 0, \quad (43)$$

whence, after defining the energy norm as $E(t) = 1/2 \langle u, u \rangle$, taking the inner product with u , and using the SBP property, one obtains

$$\frac{dE}{dt} = \frac{\lambda}{2} u_1^2 - \frac{\lambda}{2} u_N^2. \quad (44)$$

The simplest instance of SBP operator is obtained by coupling central second-order differencing at the interior of the domain with one-sided derivative closures, and appropriate choice of the norm matrix

$$D = \frac{1}{h} \begin{pmatrix} -1 & 1 & & & \\ -0.5 & 0 & 0.5 & & \\ & \ddots & \ddots & \ddots & \\ & & -0.5 & 0 & 0.5 \\ & & & -1 & 1 \end{pmatrix}, \quad H = h \begin{pmatrix} 0.5 & & & & \\ & 1 & & & \\ & & \ddots & & \\ & & & 1 & \\ & & & & 0.5 \end{pmatrix}. \quad (45)$$

It is noteworthy that the discrete energy estimate (44) was obtained without imposing any boundary condition. In the case that a boundary condition is imposed at the left boundary, $u_1(t) = f(t)$, stability can be guaranteed by augmenting Eq. (43) with a relaxation term

$$u_t + \lambda Du = -\lambda \frac{\tau}{2} H^{-1} s (u_1 - f(t)), \quad (46)$$

where $s_i = \delta_{i1}$, and τ is a suitable nondimensional relaxation constant. Notably, the correction given by Eq. (46) shall be applied at several near-boundary nodes, for general H matrices. Application of the SBP machinery yields, in the case of homogeneous boundary conditions, the energy estimate

$$\frac{dE}{dt} = -\frac{\lambda}{2} u_N^2 - \frac{\lambda}{2} u_1^2 (\tau - 1), \quad (47)$$

which shows that the method is time stable if $\tau \geq 1$.

The characteristic relaxation method given by Eq. 16 in the case of the linear advection equation amounts to replacing the discretized equation at the first node with

$$\frac{du_1}{dt} = -\frac{\lambda}{h} (u_1 - f(t + h/\lambda)), \quad (48)$$

where we have accounted for the fact that the exact solution at the ghost point is given by $u^*(-h, t) = u^*(0, t + h/\lambda) = f(t + h/\lambda)$, and the overall semi-discrete difference scheme can then be cast in vector form as

$$u_t + \lambda Du = -\lambda s \left((Du)_1 - \frac{1}{h} (u_1 - f(t)) \right). \quad (49)$$

The main differences with respect to Eq. (46) are as follows: (i) in GRCBC the damping terms replace the right-hand-side, whereas in the classical formulation of SBP-SAT the damping terms are added to the right-hand-side of the equations (but see Berg and Nordström [33] for an alternative formulation of SAT in which the equations are not solved at the boundary); (ii) in GRCBC the driving term is the target value of the solution at a point outside the computational domain, whereas in SBP-SAT the relaxation is carried out point-wise; (iii) in GRCBC, the equations are modified at the very first grid point, whereas for general non-diagonal norms SBP-SAT requires modification as several near-boundary nodes.

Eq. (48) also implies that, in the case of homogeneous boundary conditions, the discrete solution at the boundary node goes to zero as

$$u_1 \sim \exp(-t\lambda/h). \quad (50)$$

Unlike for the case of SAT closures, energy stability does not necessarily follow here, as the selected boundary closure spoils the SBP property of the difference operator. However, assuming that D has the SBP property (even though this is not strictly needed in the present approach), and that the norm matrix is diagonal, it easily follows that, for homogeneous boundary conditions

$$\frac{dE}{dt} = -\frac{\lambda}{2} u_N^2 + \frac{\lambda}{2} u_1^2 \left(1 - 2\frac{H_{11}}{h} + 2H_{11}D_{11} \right) + \lambda u_1 H_{11} \sum_{j=2}^N D_{1j} u_j. \quad (51)$$

Time stability requires that both terms at the right-hand side of Eq. (51) are negative. Negativity of the first term for a given SBP operator can be checked on a case-by-case basis, and this is for instance the case of the operator given in Eq. (45), for which the coefficient under parentheses is -1 . While the third term can be in general positive, it is expected to decay in time based on Eq. (50), which at least guarantees bounded growth of the energy norm.

Even though the theoretical support for stability is somewhat more tenuous than for the SBP-SAT approach, we have found the characteristic relaxation method here proposed to be robust in practice.

References

- [1] T. Colonius, Modeling artificial boundary conditions for compressible flow, *Annu. Rev. Fluid Mech.* 36 (2004) 315–345.
- [2] K.W. Thompson, Time dependent boundary conditions for hyperbolic systems, *J. Comput. Phys.* 68 (1988) 1–24.
- [3] T.S. Poinso, S.K. Lele, Boundary conditions for direct simulations of compressible viscous flows, *J. Comput. Phys.* 101 (1992) 104–129.
- [4] G. Lodato, P. Domingo, L. Vervisch, Three-dimensional boundary conditions for direct and large-eddy simulation of compressible viscous flows, *J. Comput. Phys.* 227 (2008) 5105–5143.
- [5] D. Rudy, J. Strikwerda, A nonreflecting outflow boundary condition for subsonic Navier–Stokes calculations, *J. Comput. Phys.* 36 (1980) 55–70.
- [6] C. Yoo, Y. Wang, A. Troune, H. Im, Characteristic boundary conditions for direct simulations of turbulent counterflow flames, *Comb. Theory Model.* 9 (2005) 617–646.
- [7] W. Polifke, C. Wall, P. Moin, Partially reflecting and non-reflecting boundary conditions for simulation of compressible viscous flow, *J. Comput. Phys.* 213 (2006) 437–449.
- [8] N. Guézennec, T. Poinso, Acoustically nonreflecting and reflecting boundary conditions for vorticity injection in compressible solvers, *AIAA J.* 47 (2009) 1709–1722.
- [9] J. Kim, D. Lee, Generalized characteristic boundary conditions for computational aeroacoustics, *AIAA J.* 38 (2000) 2040–2049.
- [10] T. Colonius, S. Lele, P. Moin, Boundary conditions for direct computation of aerodynamic sound generation, *AIAA J.* 31 (1993) 1574–1582.
- [11] T. Colonius, H. Ran, Analysis and optimization of numerical sponge layers as a nonreflective boundary treatment, *J. Comput. Phys.* 182 (2002) 191–212.
- [12] M. Israeli, S. Orszag, Approximation of radiation boundary conditions, *J. Comput. Phys.* 41 (1981) 115–135.
- [13] J. Freund, Noise sources in a low-Reynolds-number turbulent jet at Mach 0.9, *J. Fluid Mech.* 438 (2001) 277–305.
- [14] D. Bodony, Analysis of sponge zones for computational fluid mechanics, *J. Comput. Phys.* 212 (2006) 681–702.
- [15] A. Mani, Analysis and optimization of numerical sponge layers as a nonreflective boundary treatment, *J. Comput. Phys.* 231 (2012) 704–716.
- [16] M. Giles, Non-reflecting boundary conditions for the euler equations, *Tech. Rep. TR 88-1*, Massachusetts Institute of Technology (1988).
- [17] M.H. Carpenter, D. Gottlieb, S. Abarbanel, Time-stable boundary conditions for finite-difference schemes solving hyperbolic systems: methodology and application to high-order compact schemes, *J. Comput. Phys.* 111 (1994) 220–236.
- [18] M. Svård, M.H. Carpenter, J. Nordström, A stable high-order finite difference scheme for the compressible Navier–Stokes equations, far-field boundary conditions, *J. Comput. Phys.* 225 (2007) 1020–1038.
- [19] M. Svård, J. Nordström, A stable high-order finite difference scheme for the compressible navierstokes equations. No-slip wall boundary conditions, *J. Comput. Phys.* 227 (2008) 4805–4824.
- [20] D. Bodony, Accuracy of the simultaneous-approximation-term boundary condition for time-dependent problems, *J. Sci. Comput.* 43 (2010) 118–133.
- [21] L. Selle, F. Nicoud, T. Poinso, Actual impedance of nonreflecting boundary conditions: Implications for computation of resonators, *AIAA J.* 42 (2004) 958–964.
- [22] S. Pirozzoli, Generalized conservative approximations of split convective derivative operators, *J. Comput. Phys.* 229 (2010) 7180–7190.
- [23] S. Pirozzoli, P. Orlandi, M. Bernardini, The fluid dynamics of rolling wheels at low reynolds number, *J. Fluid Mech.* 706 (2012) 496–533.
- [24] N. Curle, The influence of solid boundaries upon aerodynamic sound, *Proc. R. Soc. Lond. A* 231 (1955) 505–513.
- [25] P. Spalart, Direct numerical simulation of a turbulent boundary layer up to $Re_\theta = 1410$, *J. Fluid Mech.* 187 (1988) 61–98.
- [26] J. Komminao, M. Skote, Reynolds stress budgets in Couette and boundary layer flows, *Flow Turbul. Combust.* 68 (2002) 167–192.
- [27] G. Khujadze, M. Oberlack, DNS and scaling laws from new symmetry groups of ZPG turbulent boundary layer flow, *Theor. Comput. Fluid Dyn.* 18 (2004) 391–411.
- [28] M.P. Simens, J. Jimnez, S. Hoyas, Y. Mizuno, A high-resolution code for turbulent boundary layers, *J. Comput. Phys.* 228 (2009) 4218–4231.
- [29] P. Schlatter, R. Örlü, Assessment of direct numerical simulation data of turbulent boundary layers, *J. Fluid Mech.* 659 (2010) 116–126.
- [30] X. Wu, P. Moin, Direct numerical simulation of turbulence in a nominally zero-pressure-gradient flat-plate boundary layer, *J. Fluid Mech.* 630 (2009) 5–41.

- [31] T. Lund, X. Wu, K. Squires, Generation of turbulent inflow data for spatially-developing boundary layer simulations, *J. Comput. Phys.* 140 (1998) 233–258.
- [32] S. Pirozzoli, M. Bernardini, Turbulence in supersonic boundary layers at moderate Reynolds number, *J. Fluid Mech.* 688 (2011) 120–168.
- [33] J. Berg, J. Nordström, Spectral analysis of the continuous and discretized heat and advection equation on single and multiple domains, *Appl. Numer. Math.* 62 (2012) 1620–1638.